

KOI-3278: A Self-Lensing Binary Star System

Ethan Kruse^{1*} and Eric Agol¹

¹Department of Astronomy, University of Washington,
Box 351580, Seattle, WA 98195, USA.

*Corresponding author. E-mail: eakruse@uw.edu

Over 40% of Sun-like stars are bound in binary or multistar systems. Stellar remnants in edge-on binary systems can gravitationally magnify their companions, as predicted 40 years ago. By using data from the Kepler spacecraft, we report the detection of such a “self-lensing” system, in which a 5-hour pulse of 0.1% amplitude occurs every orbital period. The white dwarf stellar remnant and its Sun-like companion orbit one another every 88.18 days, a long period for a white dwarf-eclipsing binary. By modeling the pulse as gravitational magnification (microlensing) along with Kepler’s laws and stellar models, we constrain the mass of the white dwarf to be $\sim 63\%$ of the mass of our Sun. Further study of this system, and any others discovered like it, will help to constrain the physics of white dwarfs and binary star evolution.

Einstein’s general theory of relativity predicts that gravity can bend light and, consequently, that massive objects can distort and magnify more distant sources (1). This lensing effect provided one of the first confirmations of general relativity during a solar eclipse (2). Gravitational lensing has since become a widely used tool in astronomy to study galactic dark matter, exoplanets, clusters, quasars, cosmology, and more (3, 4). One application has yet to be realized: in 1973, André Maeder predicted that binary star systems in which one star is a degenerate, compact object – a white dwarf, neutron star, or black hole – could cause repeated magnification of its companion star (instead of the standard eclipses) if the orbit happened to be viewed edge-on (5). The magnification of these self-lensing binary systems is small, typically a part in one thousand or less if the companion is Sun-like, and so it was not until high-precision stellar photometry was made possible with the Corot and Kepler spacecrafts that this could be detected (6, 7). Stellar evolution models predict that about a dozen self-lensing binaries could be found by the Kepler spacecraft (8), but none have been discovered to date. A self-lensing binary system allows the measurement of the mass of the compact object, which is not true for most galaxy-scale microlensing events in which there is a degeneracy between the velocity, distance, and mass of the lensing object (9). Microlensing does affect several known white dwarfs

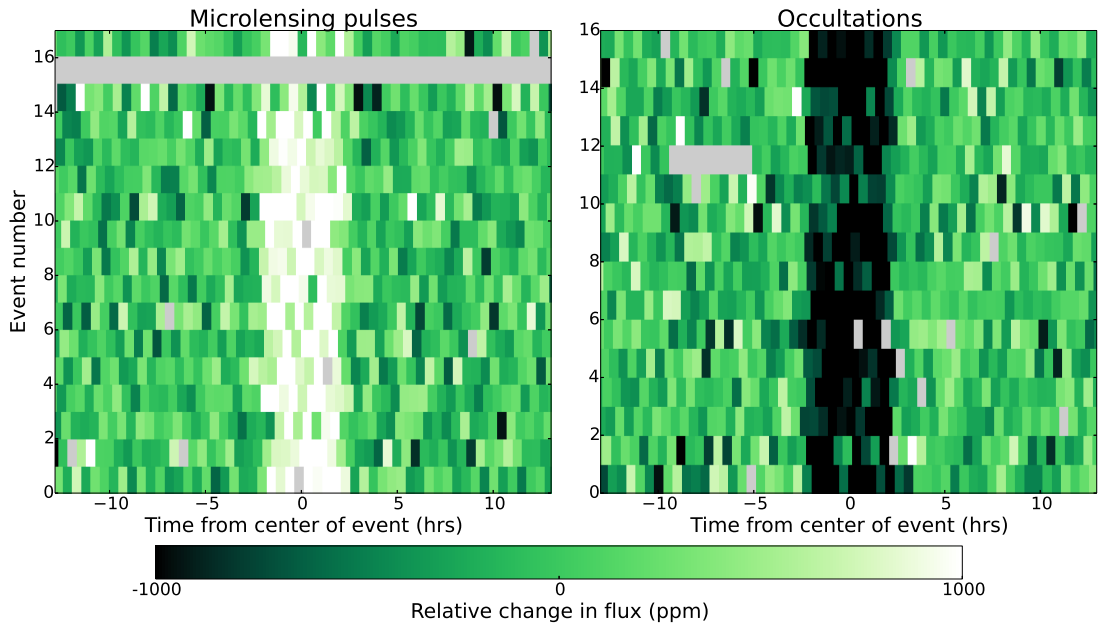


Fig. 1. Detrended flux versus time for all 16 microlensing pulses and 16 occultations in KOI-3278. Each row depicts the relative fluxes in 29.3-min Kepler cadences around an event. The rows are separated by the orbital period, $P = 88.18$ days. White represents brighter flux and black dimmer, whereas gray represents missing data or outliers that have been removed. ppm, parts per million.

in binaries in which the depth of eclipse is made slightly shallower ($10\text{--}14$) but does not result in brightening because occultation dominates over magnification at the short orbital periods of those systems.

Here, we report that Kepler Object of Interest 3278 (KOI-3278) (*15, 16*), a term intended for planetary candidates, is instead a self-lensing binary composed of a white dwarf star orbiting a Sun-like star. The candidate planetary transit signal is actually the repeated occultation of the white dwarf as it passes behind its stellar companion. A search for other planets in this system with the Quasiperiodic Automated Transit Search algorithm (*17*) turned up a series of symmetric pulses, brightenings rather than dimmings, with a near-identical period and duration as the transit candidate but occurring almost half an orbital period later. All these properties can be explained by magnification of the Sun-like star as the white dwarf passes in front; 16 microlensing pulses were found, in addition to 16 occultations. The pulses and occultations are periodic and uniform in magnitude and duration (Fig. 1), which is consistent with a nearly circular, Keplerian orbit. Because there is no other phenomenon (that we know of) that can cause such a brief, symmetric, periodic brightening, we constructed a model for KOI-3278 composed of an eclipsing white dwarf and G dwarf (Sun-like star) binary (*18*).

Even without a full model, an estimate of the mass of the white dwarf, M_2 , can be made directly from the light curve. The ratio of the fluence of the microlensing pulse, F_{pulse} , to the stellar fluence over an orbital period, F_{tot} , is given (*19*) by $F_{\text{pulse}}/F_{\text{tot}} = 5.4 \times 10^{-6} \sqrt{(1-b^2)} (M_2/M_\odot) (R_\odot/R_1)$, where R_1 is the radius of the G dwarf and b is the impact parameter (*20*). Because the duration

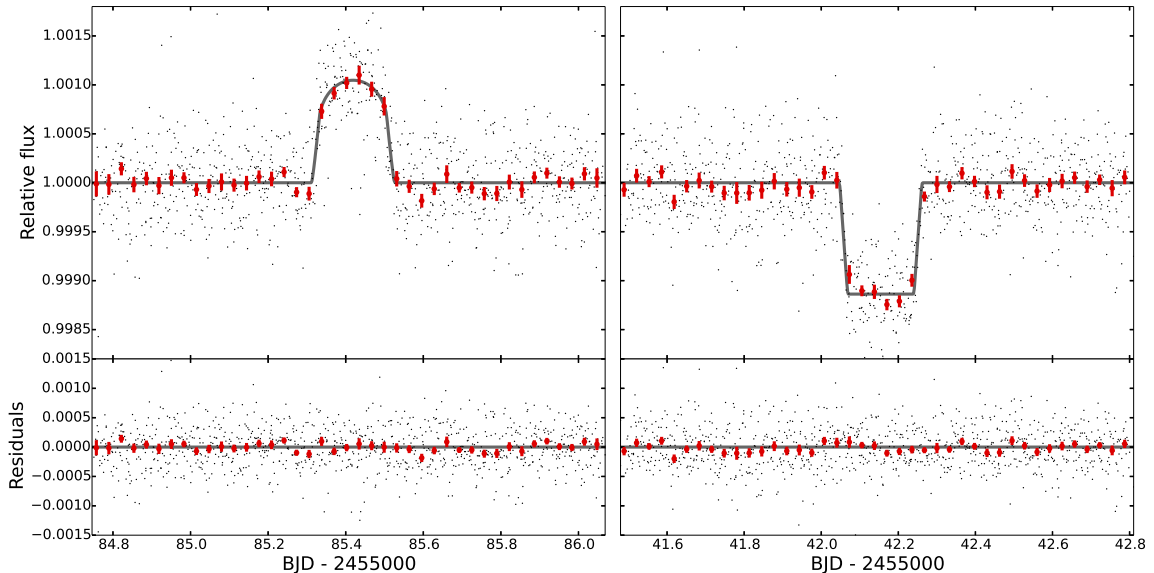


Fig. 2. Model fit to the data. Detrended and folded Kepler photometry of KOI-3278 presented as black points (all pulses and occultations have been aligned), overplotted with the best-fit model (gray line) for the microlensing pulse (**left**) and occultation (**right**). Red error bars show the mean of the folded data over a 45-min time scale. Bottom graphs show the residuals of the data with the best-fit model subtracted. BJD, barycentric Julian date.

of the pulse is 5 hours, the period is 88.18 days, and the magnification is 10^{-3} , we calculated $F_{\text{pulse}}/F_{\text{tot}}[1 - (b/0.7)^2]^{-1/2} \approx 3.3 \times 10^{-6}$ and $M_2 \approx 0.6M_{\odot}$, which is a typical mass for a white dwarf star (21).

To jointly constrain the parameters of both stars, we fitted a full model simultaneously to the Kepler time-series photometry and the multiband photometry collected from other surveys (18). We modeled the light curve by using a Keplerian orbit with the gravitational lensing approximated as an inverted transit light curve, which is appropriate when the Einstein radius is small (19). We compared the Padova stellar evolution models (22) to the multiband photometry to constrain the properties of the G dwarf while accounting for extinction, A_V . Last, we used cooling models to constrain the age of the white dwarf (23).

Our model provides an accurate description of the data (Fig. 2) with a reduced χ^2 value of unity. From this model, we calculated the stellar parameters and the binary system's orbital properties (Table 1), with uncertainties derived from a Markov-chain Monte Carlo analysis (18). The model produced a white dwarf mass of $M_2 = 0.63M_{\odot} \pm 0.05M_{\odot}$, with a G dwarf companion of $M_1 = 1.04^{+0.03}_{-0.06}M_{\odot}$, $R_1 = 0.96^{+0.03}_{-0.05}R_{\odot}$, and effective temperature $T_{\text{eff},1} = 5568 \pm 39$ K: a star very similar to our Sun. Because the white dwarf, with its small size, is much fainter than the G dwarf, we cannot yet measure its temperature directly. However, given the measured mass from gravitational lensing, we inferred its size to be $R_2 = 0.0117R_{\odot} \pm 0.0006R_{\odot}$ by using a mass-radius relation appropriate for carbon-oxygen white dwarfs. With a radius for the white dwarf, the measured occultation depth when it passes behind the G dwarf can be used to

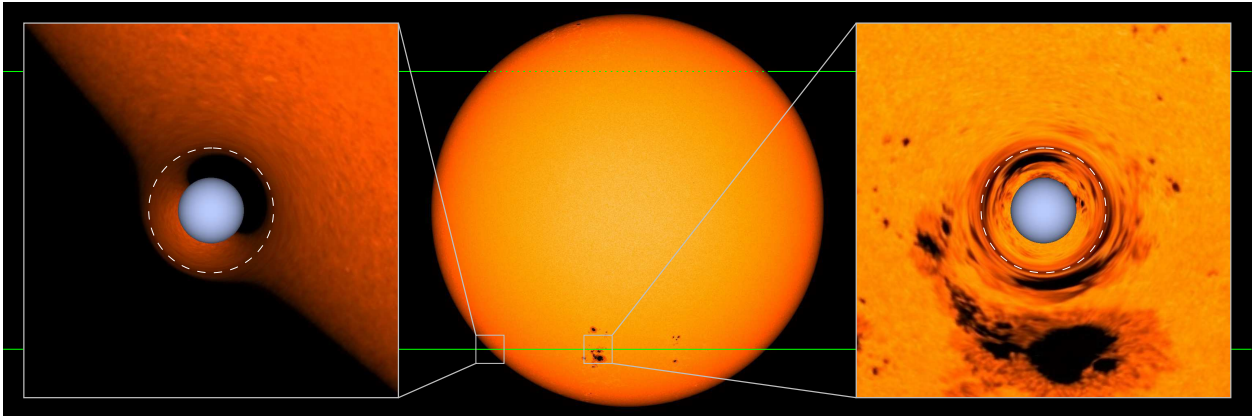


Fig. 3. Illustration of lensing magnification. (Center) The false-color disk of a G dwarf (using an actual image of the Sun from NASA/SDO HMI), in which the green line shows the trajectory of the white dwarf, with the dotted portion indicating where it passes behind the G dwarf. (Left and right) Close-ups of areas boxed in center show the lensed image of the G dwarf at two different times during the microlensing pulse; the white dwarf is the blue sphere. The white dashed line shows the Einstein ring of the white dwarf. The model that we fit to the data does not contain spots; however, the spots and granulation make the lensing distortion more apparent.

constrain the temperature of the white dwarf, which we found to be $T_{\text{eff},2} = 10,000 \pm 750$ K; this temperature would give the white dwarf the bluish hue of an A star. The Einstein radius, R_E , is about twice the inferred size of the white dwarf, which allows lensing to dominate over occultation when the white dwarf passes in front. Gravitational lensing causes a distorted and magnified image of the G dwarf outside the Einstein ring in addition to a second inverted and reflected image of the G dwarf within the Einstein ring (Fig. 3); the inner image is partially occulted by the white dwarf's disk, reducing the observed magnification slightly.

Our model does not include the effect of star spots, but the Kepler G dwarf light curve displays their characteristic quasi-periodic fluctuations with a root mean square of 0.76%. We estimated that the spots would affect the derived stellar properties by less than a percent, smaller than the statistical errors in our model. Spot analysis revealed a G dwarf rotational period of $P_{\text{rot}} = 12.5 \pm 0.1$ days. This short rotational period is expected for a G dwarf of only 0.89 ± 0.14 Gy (18). The white dwarf cooling time is $t_{\text{cool}} = 0.66 \pm 0.06$ Gy, which when added to the main sequence lifetime, t_2 , of its progenitor with mass $M_{2,\text{init}}$ gives a total age of the binary system of $t_1 = 1.6_{-0.6}^{+0.9}$ Gy; this age is marginally inconsistent (1.4σ) with the spin-down age of the G dwarf.

However, the G dwarf may have been spun up because of accretion of gas from the white dwarf progenitor. Because the white dwarf progenitor was previously a red giant, it should have enveloped the G dwarf during a common envelope phase (24). The initial orbital period of the binary was likely several years long, and the period was likely shortened because of drag during the common-envelope phase. During this phase, the G dwarf accreted some gas from the red giant, increasing its mass by 10^{-3} to $10^{-2}M_{\odot}$ and spinning the G dwarf up from the angular momentum contained in the accreted gas; this spin-up would have reset the age-spin relation, which could explain the slight age discrepancy.

Table 1: **Parameters of the KOI-3278 binary star system.** More information can be found in the supplementary text. The median and 68.3% bounds are given for each parameter. g_1 , surface gravity in cm/s^2 . L_{WD} , luminosity of the white dwarf. e , eccentricity. ω , argument of periastron. a , semi-major axis. i , inclination. F_2/F_1 , flux ratio between the white dwarf and G dwarf in the Kepler band. D , distance. σ_{sys} , systematic errors in the multiband photometry.

<i>G dwarf:</i>	
$M_1(M_\odot)$	$1.042^{+0.028}_{-0.058}$
$R_1(R_\odot)$	$0.964^{+0.034}_{-0.054}$
$[Fe/H]_1$	$0.39^{+0.22}_{-0.22}$
t_1 (Gyr)	$1.62^{+0.93}_{-0.55}$
$T_{eff,1}$ (K)	5568^{+40}_{-38}
$\log(g_1)$	$4.485^{+0.026}_{-0.020}$
<i>White dwarf:</i>	
$M_{2,init}(M_\odot)$	$2.40^{+0.70}_{-0.53}$
$M_2(M_\odot)$	$0.634^{+0.047}_{-0.055}$
$T_{eff,2}$ (K)	9960^{+700}_{-760}
$R_2(R_\odot)$	$0.01166^{+0.00069}_{-0.00056}$
$R_E(R_\odot)$	$0.02305^{+0.00093}_{-0.00107}$
t_2 (Gyr)	$0.96^{+0.90}_{-0.53}$
t_{cool} (Gyr)	$0.663^{+0.065}_{-0.057}$
$L_{WD}(L_\odot)$	$0.00120^{+0.00024}_{-0.00023}$
<i>Binary system:</i>	
P (d)	$88.18052^{+0.00025}_{-0.00027}$
t_0 (-2,455,000 BJD)	$85.4190^{+0.0023}_{-0.0023}$
$e \cos \omega$	$0.014713^{+0.000047}_{-0.000061}$
$e \sin \omega$	$0.000^{+0.049}_{-0.054}$
a (AU)	$0.4605^{+0.0064}_{-0.0103}$
a/R_1	$102.8^{+3.7}_{-2.4}$
b_0	$0.706^{+0.020}_{-0.025}$
i (deg)	$89.607^{+0.026}_{-0.020}$
F_2/F_1	$0.001127^{+0.000039}_{-0.000039}$
D (pc)	808^{+36}_{-49}
σ_{sys}	$0.0246^{+0.0127}_{-0.0078}$
K_1 (km/s)	$21.53^{+0.96}_{-0.98}$
π (milli-arc sec)	$1.237^{+0.079}_{-0.053}$
α_1 (milli-arc sec)	$0.2169^{+0.0076}_{-0.0072}$
A_V (mags)	$0.206^{+0.017}_{-0.016}$

KOI-3278 is the longest period eclipsing post-common-envelope binary found to date (fig. S7), and it is also one of the only examples of an eclipsing Sirius-like system – a binary composed of a non-interacting white dwarf and a Sun-like (or hotter) main-sequence star (25–27). As such, it will help to provide constraints on the physics of formation and evolution of short and intermediate period evolved binary stars, thereby improving our knowledge of the formation of accreting binaries and sources of gravitational waves. We expect that a few more self-lensing binaries will be found in the Kepler data at shorter orbital periods than KOI-3278. The magnification decreases down to periods of ≈ 16 days, making them more difficult to find; at even shorter periods, occultation by the white dwarfs disk wins out over the lensing, causing a shallower eclipse as in KOI-256 (13). Systems like KOI-3278 should not be a substantial source of false-positives for exoplanets; only one was predicted to be found in the Kepler data with its magnification of $\approx 0.1\%$ (8).

Follow-up observations should better constrain the parameters of the white dwarf star in KOI-3278, allowing a test of the mass-radius relation for white dwarfs (28, 29). Once the Kepler field rises (it had set before we detected the microlensing signal), radial velocity observations should show a semi-amplitude of $K_1 = 21.5$ km/s and a line-broadening of 4 km/s. High-resolution spectroscopy will also better constrain the atmospheric properties of the G dwarf; in particular, spectral abundance anomalies caused by accretion of nuclear-processed material from the white dwarf progenitor should be sought. Measurements of the occultation of the white dwarf in the ultraviolet (with the Hubble Space Telescope) should appear much deeper, as much as 60% in depth as opposed to the 0.1% occultation depth in the Kepler band, and will yield constraints on the radius and temperature of the white dwarf. High angular resolution imaging would allow for better constraints to be placed on the presence of a third star in the system (18). Last, parallax measurements, π , with the Gaia spacecraft (30) will improve the precision of the properties of the G dwarf; Gaia can also detect the reflex motion, α_1 , of the G dwarf as it orbits the center of mass with the white dwarf. This provides another means to detect systems like KOI-3278 with inclinations that do not show microlensing or occultation; there are likely 100 of these among the Kepler target stars alone, given the 1% geometric lensing probability of KOI-3278.

References and Notes

1. A. Einstein, *Science* **84**, 506-507 (1936).
2. F. W. Dyson, A. S. Eddington, C. Davidson, *Philos. Trans. R. Soc. London Ser. A* **220**, 291-333 (1920).
3. J. Wambsganss, *Living Reviews in Relativity* **1**, 12 (1998).
4. P. Schneider, C. Kochanek, J. Wambsganss, *Gravitational Lensing: Strong, Weak and Micro* (Saas-Fee Advanced Course 33, Springer, Berlin, 2006).
5. A. Maeder, *Astron. Astrophys.* **26**, 215 (1973).
6. E. Agol, *Astrophys. J.* **579**, 430-436 (2002).
7. K. C. Sahu, R. L. Gilliland, *Astrophys. J.* **584**, 1042-1052 (2003).
8. A. J. Farmer, E. Agol, *Astrophys. J.* **592**, 1151-1155 (2003).

9. B. Paczynski, *Annu. Rev. Astron. Astrophys.* **34**, 419-459 (1996).
10. T. R. Marsh, *Mon. Not. R. Astron. Soc.* **324**, 547-552 (2001).
11. J. D. R. Steinfadt, et al., *Astrophys. J.* **716**, L146-L151 (2010).
12. J. F. Rowe, et al., *Astrophys. J.* **713**, L150-L154 (2010).
13. P. S. Muirhead, et al., *Astrophys. J.* **767**, 111 (2013).
14. D. L. Kaplan, et al., *Astrophys. J.* **780**, 167 (2014).
15. C. J. Burke, et al., *Astrophys. J. Suppl. Ser.* **210**, 19 (2014).
16. P. Tenenbaum, et al., *Astrophys. J. Suppl. Ser.* **211**, 6 (2014).
17. J. A. Carter, E. Agol, *Astrophys. J.* **765**, 132 (2013).
18. Materials and methods are available as supplementary materials on *Science Online*.
19. E. Agol, *Astrophys. J.* **594**, 449-455 (2003).
20. The impact parameter is the projected sky separation of the white dwarf and G dwarf at midpulse, in units of the radius of the G dwarf; we find a best-fit value of $b = 0.7$ based on the full model fit. This formula assumes a circular orbit, neglects limb-darkening, and neglects obscuration by the white dwarf; whereas these effects (although minor) are accounted for in our full model.
21. S. O. Kepler, et al., *Mon. Not. R. Astron. Soc.* **375**, 1315-1324 (2007).
22. A. Bressan, et al., *Mon. Not. R. Astron. Soc.* **427**, 127-145 (2012).
23. P. Bergeron, et al., *Astrophys. J.* **737**, 28 (2011).
24. N. Ivanova, et al., *Astron. Astrophys. Review* **21**, 59 (2013).
25. A. Rebassa-Mansergas, et al., *Mon. Not. R. Astron. Soc.* **423**, 320-327 (2012).
26. M. Zorotovic, M. R. Schreiber, *Astron. Astrophys.* **549**, A95 (2013).
27. J. B. Holberg, et al., *Mon. Not. R. Astron. Soc.* **435**, 2077-2091 (2013).
28. J. L. Provencal, H. L. Shipman, E. Hog, P. Thejll, *Astrophys. J.* **494**, 759 (1998).
29. S. G. Parsons, et al., *Mon. Not. R. Astron. Soc.* **420**, 3281-3297 (2012).
30. M. A. C. Perryman, et al., *Astron. Astrophys.* **369**, 339-363 (2001).
31. A. Gould, *Astrophys. J.* **446**, 541 (1995).
32. S. Rahvar, A. Mehrabi, M. Dominik, *Mon. Not. R. Astron. Soc.* **410**, 912-918 (2011).
33. S. Mao, *Research in Astron. Astrophys.* **12**, 947-972 (2012).

34. R. Di Stefano, *Astron. J.* **141**, 142 (2011).
35. J. N. Winn, in *Exoplanets*, S. Seager, Ed. (Univ. of Arizona Press, Tucson, 2011), pp.55-77.
36. K. Mandel, E. Agol, *Astrophys. J.* **580**, L171-L175 (2002).
37. D. Heyrovsky, A. Loeb, *Astrophys. J.* **490**, 38 (1997).
38. D. K. Sing, *Astron. Astrophys.* **510**, A21 (2010).
39. A. Loeb, B. S. Gaudi, *Astrophys. J.* **588**, L117-L120 (2003).
40. S. Zucker, T. Mazeh, T. Alexander, *Astrophys. J.* **670**, 1326-1330 (2007).
41. W. F. Welsh, et al., *Astrophys. J. Suppl. Ser.* **197**, 4 (2011).
42. S. E. Thompson, et al., *Astrophys. J.* **753**, 86 (2012).
43. J. Z. Gazak, et al., *Adv. Astron.* **2012**, 1-8 (2012).
44. J. A. Carter, J. N. Winn, *Astrophys. J.* **704**, 51-67 (2009).
45. A. Dotter, et al., *Astrophys. J. Suppl. Ser.* **178**, 89-101 (2008).
46. M. H. Pinsonneault, et al., *Astrophys. J. Suppl. Ser.* **199**, 30 (2012).
47. D. Huber, et al., *Astrophys. J. Suppl. Ser.* **211**, 2 (2014).
48. K. N. Abazajian, et al., *Astrophys. J. Suppl. Ser.* **182**, 543-558 (2009).
49. R. M. Cutri, et al., VizieR Online Data Catalog: II/246 (2003).
50. R. M. Cutri, et al., VizieR Online Data Catalog: II/311 (2012).
51. E. F. Schlafly, D. P. Finkbeiner, *Astrophys. J.* **737**, 103 (2011).
52. D. O. Jones, A. A. West, J. B. Foster, *Astron. J.* **142**, 44 (2011).
53. J. Eastman, B. S. Gaudi, E. Agol, *Publ. Astron. Soc. Pac.* **125**, 83-112 (2013).
54. J. Goodman, J. Weare, *Communications in Applied Mathematics and Computational Science* **5**, 65-80 (2010).
55. D. Foreman-Mackey, D. W. Hogg, D. Lang, J. Goodman, *Publ. Astron. Soc. Pac.* **125**, 306-312 (2013).
56. T. Reinhold, A. Reiners, G. Basri, *Astron. Astrophys.* **560**, A4 (2013).
57. E. E. Mamajek, L. A. Hillenbrand, *Astrophys. J.* **687**, 1264-1293 (2008).
58. V. Weidemann, *Astron. Astrophys.* **363**, 647-656 (2000).
59. J. S. Kalirai, et al., *Astrophys. J.* **676**, 594-609 (2008).

60. O. De Marco, et al., *Mon. Not. R. Astron. Soc.* **411**, 2277-2292 (2011).
61. S. Catalán, et al., *Astron. Astrophys.* **477**, 213-221 (2008).
62. J. K. Zhao, et al., *Astrophys. J.* **746**, 144 (2012).
63. J. B. Holberg, P. Bergeron, *Astron. J.* **132**, 1221-1233 (2006).
64. P. M. Kowalski, D. Saumon, *Astrophys. J.* **651**, L137-L140 (2006).
65. P. E. Tremblay, P. Bergeron, A. Gianninas, *Astrophys. J.* **730**, 128 (2011).
66. T. M. Brown, D. W. Latham, M. E. Everett, G. A. Esquerdo, *Astron. J.* **142**, 112 (2011).
67. C. A. Tout, S. J. Aarseth, O. R. Pols, P. P. Eggleton, *Mon. Not. R. Astron. Soc.* **291**, 732 (1997).
68. J. R. Hurley, O. R. Pols, C. A. Tout, *Mon. Not. R. Astron. Soc.* **315**, 543-569 (2000).
69. J. R. Hurley, C. A. Tout, O. R. Pols, *Mon. Not. R. Astron. Soc.* **329**, 897-928 (2002).
70. B. Paczynski, *Structure and Evolution of Close Binary Systems* **73**, 75 (1976).
71. I. Iben Jr., M. Livio, *Publ. Astron. Soc. Pac.* **105**, 1373-1406 (1993).
72. M. de Kool, H. Ritter, *Astron. Astrophys.* **267**, 397-409 (1993).
73. M. de Kool, P. J. Green, *Astrophys. J.* **449**, 236 (1995).
74. P. J. Green, B. Ali, R. Napiwotzki, *Astrophys. J.* **540**, 992-1004 (2000).
75. M. R. Schreiber, B. T. Gänsicke, *Astron. Astrophys.* **406**, 305-321 (2003).
76. B. Willems, U. Kolb, *Astron. Astrophys.* **419**, 1057-1076 (2004).
77. M. Zorotovic, M. R. Schreiber, B. T. Gänsicke, A. Nebot Gómez-Morán, *Astron. Astrophys.* **520**, A86 (2010).
78. S. Toonen, G. Nelemans, *Astron. Astrophys.* **557**, A87 (2013).
79. P. J. Davis, U. Kolb, B. Willems, *Mon. Not. R. Astron. Soc.* **403**, 179-195 (2010).
80. E. B. Ford, B. Kozinsky, F. A. Rasio, *Astrophys. J.* **535**, 385-401 (2000).
81. B. Katz, S. Dong, R. Malhotra, *Phys. Rev. Lett.* **107**, 181101 (2011).
82. S. Naoz, B. Kocsis, A. Loeb, N. Yunes, *Astrophys. J.* **773**, 187 (2013).
83. J. H. J. de Bruijne, *Astrophys. Space Sci.* **341**, 31-41 (2012).
84. Pickles, A. J., A Stellar Spectral Flux Library: 1150–25000 Å, *Publ. Astron. Soc. Pac.*, **110**, 863-878 (1998).

Acknowledgments: E.K. was funded by an NSF Graduate Student Research Fellowship. E.A. acknowledges funding by NSF Career grant AST 0645416; NASA Astrobiology Institute Virtual Planetary Laboratory, supported by NASA under cooperative agreement NNH05ZDA001C; and NASA Origins of Solar Systems grant 12-OSS12-0011. Solar image courtesy of NASA/Solar Dynamics Observatory (SDO) and the Helioseismic and Magnetic Imager (HMI) science teams. The Kepler data presented in this paper were obtained from the Mikulski Archive for Space Telescopes (MAST). The code used for analysis is provided in a repository at github.com/ethankruse/koi3278. The authors welcome requests for additional information regarding the material presented in this paper.

Supplementary Materials

[www.sciencemag.org/content/344/6181/\[PAGE\]/suppl/DC1](http://www.sciencemag.org/content/344/6181/[PAGE]/suppl/DC1)

Materials and Methods

Supplementary Text

Figs. S1 to S7

Table S1

References (31–84)

10 February 2014; accepted 25 March 2014

10.1126/science.1251999

Supplementary Materials

Here we provide additional description of our methods in modeling and constraining the properties of KOI-3278.

0.1 Terminology

We use the term “self-lensing binary” to refer to a binary star system that is edge-on and in which one star causes a brightening of its companion – due to gravitational magnification, or “microlensing” – as it passes in front of the companion’s disk (7, 31–33). Since a self-lensing binary has not been detected to date, we need to define some terminology for periodic microlensing in a binary star system. In particular, the brightening that occurs in KOI-3278 when the white dwarf magnifies the G dwarf is neither an eclipse nor a transit, which are associated with a decrease in the brightness of the system. Nor can this be described as a “microlensing event” since it repeats; it is not a single event. Maeder (5) used the term “gravitational flash” to describe repeated microlensing in a binary; however, this term could also connote gravitational waves or explosive events. Others have used the term “anti-transit” (34), but this has also been used to refer to a secondary eclipse that happens opposite in the orbit to the transit (35). Instead of these terms, we refer to the series of brightenings that occur as the white dwarf magnifies the G dwarf as a “microlensing pulse train”, and to a single event as a “pulse.”

We refer to the G dwarf as the primary star and the white dwarf as the secondary, and we label their physical properties with 1 and 2; thus the masses and radii are M_1 and R_1 for the G dwarf and M_2 and R_2 for the white dwarf. We refer to the secondary eclipse, when the white dwarf passes behind the G dwarf, as the occultation.

1 Photometric time series model

1.1 Kepler photometry

We used the simple-aperture-photometry flux (SAP_FLUX) from the Kepler pipeline for all available quarters (Q1-Q17). The times are the mid-point of each cadence, converted to barycentric julian date (BJD). We rejected points that were flagged with cosmic ray contamination or single-point outliers (SAP_QUALITY flags 128 and 2048).

A plot of the pulses and occultations is shown in Figure S1.

1.2 Light curve model

We computed a light curve model for KOI-3278 (Kepler Input Catalog [KIC] number 3342467) using transiting planet modeling software developed by one of us (36), but with the sign of the flux changes switched for the microlensing pulses. This inverted-transit approximation is justified because a lensing light curve shape is well approximated by that of a transit light curve (with small deviations at ingress and egress) when the Einstein radius is much smaller than the size of the lensed source, as is the case in this system; the only difference is a transit’s loss of light becomes a corresponding addition for a lensing event with the pulse height governed by two ratios: the Einstein radius and the lensing star’s radius to the radius of the lensed source

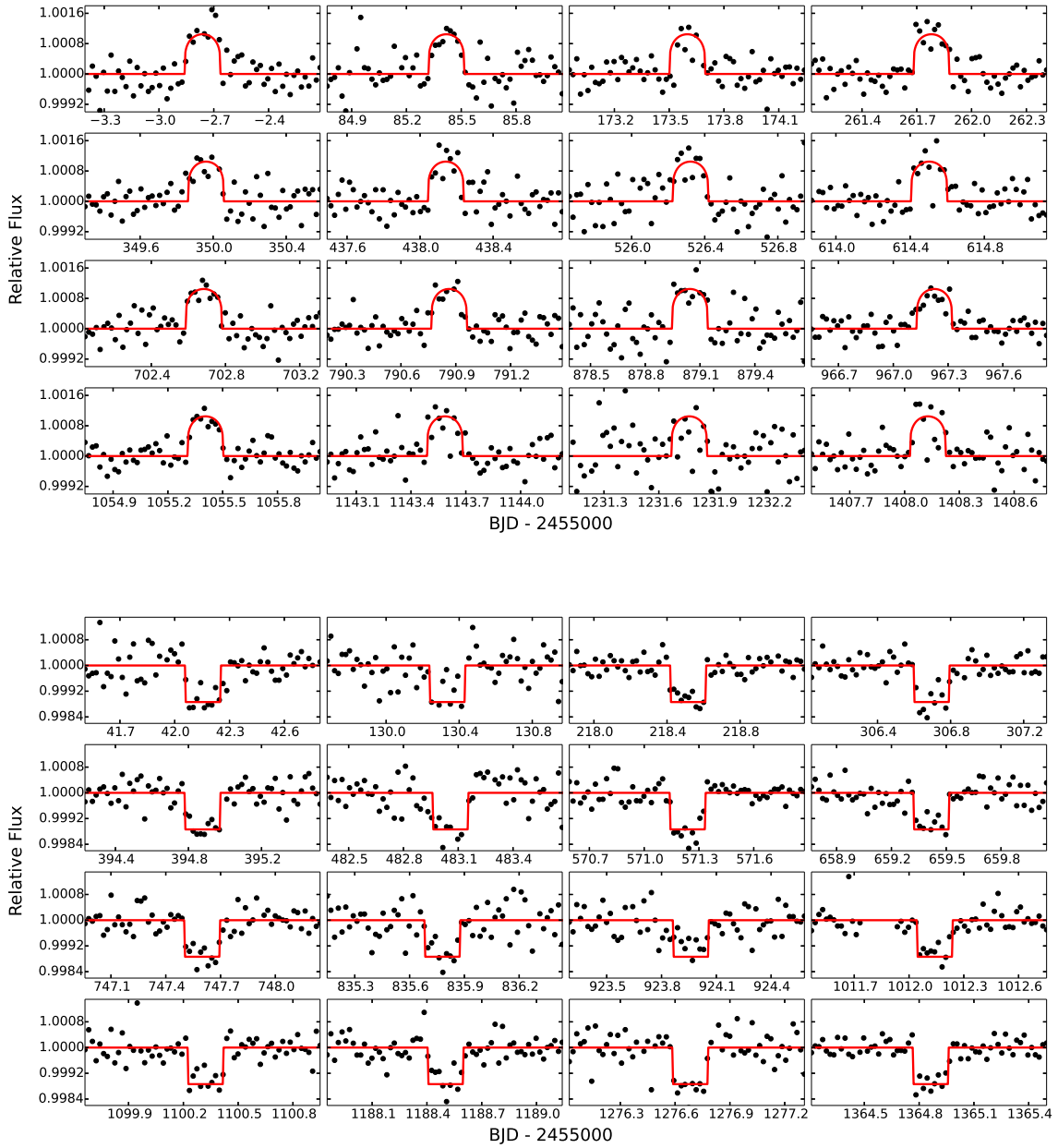


Figure S1: Detrended light curves encompassing the individual microlensing pulses (top) and occultations (bottom). The red lines show our best-fit model.

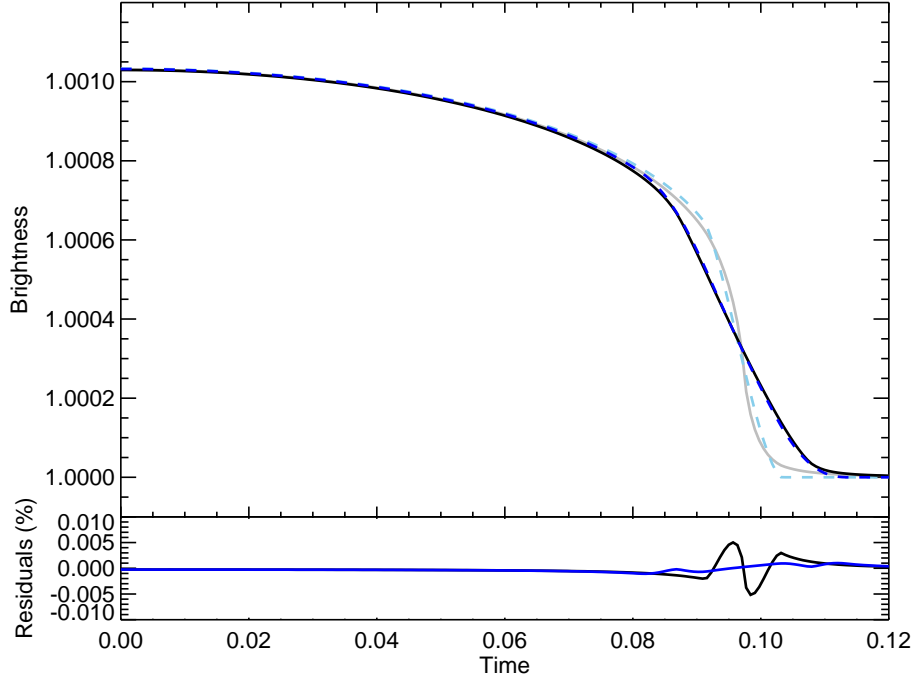


Figure S2: Comparison of the exact calculation of the microlensing pulse (6) with the inverted transit approximation (19) for the best-fit parameters of KOI-3278 (the pulse is symmetric, so we only plot the second half). Top panel: exact calculation (light grey, solid); inverted transit approximation (light blue, dashed); exact calculation convolved with Kepler long cadence (black, solid); inverted transit approximation convolved with Kepler long cadence (dark blue, dashed). Bottom panel: difference between the exact microlensing calculation and inverted transit approximation, without (black) and with (blue) convolution with the Kepler long cadence.

(19, 37). In this case the ingress and egress deviations ($\lesssim 1 \times 10^{-5}$, Figure S2) are undetectable at the level of precision of the Kepler data due to the 29.3 minute Kepler cadence. Consequently, we utilized this inverted transit approximation due to its much faster computation using analytic expression in terms of elliptic integrals (36).

To an excellent approximation then, the pulse model is described by

$$F(t) = F_1(t) \left(1 + \frac{2R_E^2 - R_2^2}{R_1^2} \cdot \frac{I_1(t)}{\langle I_1 \rangle} \right) + F_2 \quad (1)$$

where $F(t)$ is the flux from the binary system, F_1 is the unclipped G dwarf flux, F_2 is the flux from the white dwarf (assumed to be constant), R_E is the Einstein radius of the white dwarf, $I_1(t)$ is the intensity of the G dwarf at the location behind the center of the white dwarf, and $\langle I_1 \rangle$ is the disk-averaged intensity of the G dwarf (this formula applies between ingress and egress).

The specific intensity of the G dwarf in the Kepler bandpass we modeled with a quadratic limb-darkening law; initial fits confirmed that the signal to noise of the pulses was not sufficient to fit for these coefficients independently, so we instead adopted them from a tabulation for the Kepler bandpass as a function of the effective temperature, metallicity, and surface gravity of

the stellar atmosphere (38). We fitted the tabulated limb-darkening coefficients as a function of the atmospheric parameters, obtaining:

$$\begin{aligned} u_1 &= 0.4466 - 0.196 \left(\frac{T_{eff,1}}{10^3} - 5.5 \right) + 0.00692 \log_{10} \left(\frac{g_1}{10^{4.5}} \right) + 0.0865 [Fe/H]_1 \\ u_2 &= 0.2278 - 0.128 \left(\frac{T_{eff,1}}{10^3} - 5.5 \right) - 0.00458 \log_{10} \left(\frac{g_1}{10^{4.5}} \right) - 0.0506 [Fe/H]_1, \end{aligned} \quad (2)$$

where u_1, u_2 are the linear and quadratic limb-darkening coefficients, $T_{eff,1}$ is the effective temperature of the G dwarf in Kelvin, g_1 is the surface gravity of the G dwarf in cm sec^{-2} , and $[Fe/H]_1$ is the abundance ratio of iron to hydrogen, relative to the Sun, in units of dex (log base 10). This fit is valid in the range $5000 < T_{eff,1} < 6000$ K, $4 < \log_{10}(g_1) < 5$, and $-0.5 < [Fe/H]_1 < 0.5$, and is accurate to 0.005. These coefficients were used in conjunction with equation 1 to compute the light curve of the microlensing pulses, while the occultations were computed assuming a uniform flux for the white dwarf (36).

Since the G dwarf is spotted and undergoes quasi-periodic fluctuations as the spots rotate in and out of view, we modeled the $F_1(t)$ near each pulse and occultation as a quadratic function of time and subsequently marginalized over these polynomial coefficients. To speed up the modeling, we carried out a linearized fit for the polynomial coefficients of $F_1(t_i) = \sum_{j=0}^n a_j (t_i - t_j)^j$ around each event, with $n = 2$. We first computed the light curve model $F(t)$ assuming $F_1(t) = 1$ and F_2/F_1 is a constant; we then divided this model into the light curve and solved the linear least-squares problem for the a_j that minimized χ^2 , thus marginalizing over a_j . This procedure ignored the slight variation in the ratio $F_2/F_1(t)$, but since $F_2/F_1 \approx 10^{-3}$ and the variation in F_1 is a few percent at most, this error is of order 10^{-5} , which is substantially smaller than the observational uncertainties. In computing the model, we sub-sampled each data point by a factor of ten to properly resolve the ingress and egress of the microlensing pulses and occultations.

We neglected photometric Doppler shift (39), ellipsoidal variability due to tidal distortions, and reflected light from the companion star, which are only significant for binaries with short periods (40), and are swamped by the stronger stellar variability in this system. Ellipsoidal brightening can be caused by transient tidal distortion near periastron passage for highly-eccentric binaries known informally as “heartbeat stars” (41, 42); however, these brightenings are typically asymmetric and/or show nearby dips, i.e. they do not show the inverted-U shape of the pulse seen in KOI-3278. In addition, they typically occur near eclipse/occultation (if eclipsing) since the probability of eclipse is highest near periastron, while in KOI-3278 the brightening occurs opposite in phase to the occultation.

1.3 Orbital model

We modeled the orbit of the stars as a Kepler ellipse. We used the sky plane as the reference plane, and we refer the orbital elements to the G dwarf, thereby defining the longitude of periastron ω as the angle from the point the G dwarf crosses the sky plane going away from the observer to the G dwarf’s periastron. The separation between the stars, projected onto the sky, is given by:

$$r_{sky} = \frac{a(1 - e^2)}{1 + e \cos f} \sqrt{1 - \sin^2 i \sin^2(\omega + f)}, \quad (3)$$

where a is the semi-major axis, e is the orbital eccentricity, i is the orbital inclination ($i = 90^\circ$ for edge-on orbit; $i = 0^\circ$ for a face-on orbit), and f is the true anomaly. Note that since we assume a Keplerian orbit with two bodies, the orbital elements of the two stars are the same, with the exception of the longitude of periastra which differ by 180 degrees.

The microlensing pulse occurs when the white dwarf passes in front of the G dwarf; at this point the G dwarf has a true anomaly which equals $f_0 = \pi/2 - \omega$. Instead of the time of periastron as a reference time, we use the midtime of the first pulse, t_0 , as the reference time of the orbit, which is related to the time of periastron, τ , by:

$$\tau = t_0 + \sqrt{1 - e^2} \frac{P}{2\pi} \left[\frac{e \sin f_0}{(1 + e \cos f_0)} - 2\sqrt{1 - e^2} \arctan \left(\frac{\sqrt{1 - e^2} \tan(f_0/2)}{(1 + e)} \right) \right], \quad (4)$$

where P is the orbital period. To a good approximation, valid for small eccentricity, the time of occultation is given by $\delta t_{occ} \equiv t_{occ} - t_0 - \frac{P}{2} = \frac{2P}{\pi} e \cos \omega$.

2 Photometric analysis

We carried out two independent analyses of the data: 1) separate fits to the microlensing pulse train and to the occultations; 2) joint fits to the pulse train and occultations using the orbital model above. Each fit made slightly different assumptions and used separate software; a comparison of these two analyses for consistency increased our confidence in each analysis and in our inference of the parameters of the system.

2.1 Separate fits

The first set of fits used the Transit Analysis Package (TAP) (43). The pulse and occultation light curves were each computed assuming a constant velocity and straight trajectory during each pulse/occultation event; this is a good approximation due to the large orbital radius and nearly edge-on configuration. The pulses/occultations were each fit with five physical parameters: initial time of pulse/occultation, t_0 ; period, P ; impact parameter, b ; transit duration, T ; and the radius ratio, p . The impact parameter, b , is the sky-projected separation of the centers of the two stars at mid pulse/occultation, normalized to the radius of the G dwarf. The transit duration is defined to be: $T = 2R_1 \sqrt{1 - b^2}/v$, where v is the sky-velocity at mid-pulse/occultation. The radius ratio, p , is a parameter used in transit fitting, which is used to parameterize the limb-darkened microlensing pulse or occultation. In the case of the pulse, $p = -\sqrt{\frac{2R_E^2 - R_2^2}{R_1^2}}$, while in the case of the occultation, $p = \sqrt{F_2/(F_1 + F_2)}$. Negative values of p are converted into a flux brightening rather than dimming, as is appropriate for the microlensing pulses.

In the TAP analysis, the limb-darkening of the G star was described by a quadratic limb-darkening law with parameters $u_1 = 0.4451$ (linear) and $u_2 = 0.2297$ (quadratic) which were taken from a stellar atmosphere model with $T_{eff} = 5500$ K, $\log(g) = 4.5$, and $[Fe/H] = 0.0$ (38). The white dwarf was assumed to have no limb-darkening; this is a sufficient approximation since only the ingress/egress of the occultation is sensitive to the white dwarf limb-darkening, while this portion of the light curve has very low signal-to-noise due to the long Kepler cadence. In addition to the quadratic variation of the G dwarf, a correlated-noise model assuming $1/f$ noise in addition to a white-noise component was solved for along with the model parameters

Table S1: Light curve parameters

<i>Pulses:</i>	
Period (d)	88.18025 ± 0.00049
Duration (d)	0.1955 ± 0.0043
Pulse height D	0.00102 ± 0.00005
$t_0 + 7 \times P$ (JD-2,454,900)	702.68181 ± 0.00196
<i>Occultations:</i>	
Period (d)	88.18091 ± 0.00028
Duration (d)	0.1914 ± 0.0027
Occultation depth	0.00112 ± 0.00004
$t_0 + 7.5 \times P$ (JD - 2,454,900)	703.50886 ± 0.00124

(44). The red and white noise amplitudes were allowed to vary separately for each pulse and occultation.

Table S1 shows the results of the TAP fits; we fit the posterior of these parameters with a Gaussian, and report the mean and standard deviation of the Gaussian fits (each set of parameters was weakly correlated).

The ephemerides of the microlensing pulse train and the series of occultations were fit separately; we found that their periods were nearly identical, $P_{pulse} = 88.18025 \pm 0.00049$ d and $P_{occ} = 88.18091 \pm 0.00028$ d, for a difference of $P_{pulse} - P_{occ} = -0.9 \pm 0.8$ min. This indicates that both the microlensing pulse train and occultations can be described by a single, Keplerian orbital model, which justifies the joint fit in the next section. The occultation occurs $\Delta t_{occ} = t_{0,occ} - t_{0,pulse} - P/2 = 0.827 \pm 0.002$ days later than half of an orbital period after the pulse. This translates into $e \cos \omega = 0.01473 \pm 0.00004$.

We also found that the impact parameters of the pulse train and occultations were poorly constrained; only near-grazing configurations could be excluded. This is due, once again, to the long-cadence data which place no constraint on the ingress/egress duration, approximately 6 – 9 min, which is shorter than the 29.3-minute Kepler cadence. For the occultation, the TAP model was incorrect at ingress/egress in that it fixed the depth to equal the square root of the radius ratio; consequently we do not trust the impact parameter constraint on the occultation. For the pulse, the impact parameter likelihood showed a decline above an impact parameter of $b = 0.65$, which we fit with a linear decline down to $b = 1.06$.

We found that the durations of the pulses and the occultations were identical to within the errors, $T_{pulse} = 0.196 \pm 0.004$ d and $T_{occ} = 0.191 \pm 0.003$ d, for a difference of $T_{pulse} - T_{occ} = 6 \pm 7$ min and a ratio of $T_{pulse}/T_{occ} = 1.02 \pm 0.03$. A ratio near unity also indicates that both events can be described by a single Keplerian orbital model with (likely) small $x = e \sin \omega$. In theory the ratio of the durations can be used to constrain $e \sin \omega$; to lowest order in $x = e \sin \omega$: $\frac{T_{pulse}}{T_{occ}} = 1 + ax$, with $a = 2 \frac{2b_0^2(1-y^2)-1}{1-b_0^2(1-y^2)^2}$, $y = e \cos \omega$ and $b_0 = a \cos i/R_1$ (the impact parameter if $e = 0$). In the limit $b_0 = 0$, $a = -2$, which yields $e \sin \omega = -0.0035 \pm -0.016$. However, at larger impact parameter the sign of a switches, and a goes to zero for $b_0 = 1/\sqrt{2}$; near this value the x^2 term which we have dropped in T_{pulse}/T_{occ} becomes important in constraining the value of $e \sin \omega$. The best-fit impact parameter from the joint model gives $b_0 = 0.706 \pm 0.022$; this translates to $a = -0.1 \pm 0.5$, which spans zero, so $e \sin \omega$ has a larger uncertainty than this

linear expansion estimate; it is properly constrained by the full Markov chain solution.

To translate the separate constraints on the shape of the light curve into constraints on the system parameters, we next carried out an MCMC analysis using analytic formulas to describe the light curve parameters in terms of the masses, radii, and orbital parameters of the G dwarf and white dwarf (35). We found a strong correlation between T , p and b for the microlensing pulse fit, so we reparameterized p as $D(b) = p^2 \frac{1-u_1\mu-u_2\mu^2}{1-u_1/3-u_2/6}$ where $\mu = 1 - \sqrt{1-b^2}$. This parameter approximates the maximum height of the microlensing pulse, at its center, and is nearly uncorrelated with b and T . Although the TAP light curve fits held u_1 and u_2 fixed, we allowed these to vary during this second step of the analysis computing $D(b)$. We also transformed the zero-points of the ephemerides to points near the middle of the series of pulses/occultations so that they were uncorrelated with the orbital periods. The results of these fits were used for rapid experimentation with various assumptions in our analysis and comparison with the joint fits described next; however, the joint fits have the advantage of self-consistently fitting all of the data simultaneously, so we use the joint fits for our final parameter constraints.

2.2 Joint fits

The second model jointly simulated the pulses and occultations and compared to the observed Kepler fluxes near the events. Using the masses of the two bodies and their orbital elements as inputs ($M_1, M_2, P, t_0, i, e, \omega$), we calculated the two stars' projected sky separation (Equation 3) at all times of interest (i.e. Kepler cadences surrounding the pulses and occultations, subsampled by a factor of 10). We combined this sky separation with the radii of the two stars, their flux ratio, and the G-dwarf's limb darkening coefficients ($R_1, R_2, \frac{F_2}{F_1}, u_1, u_2$) to predict the observed flux at each cadence using the method of §1.2; we then calculated the χ^2 of the model with these 12 parameters.

To further constrain the system parameters and break degeneracies between them, we utilized stellar evolution models and added photometric constraints from other surveys to our χ^2 calculation, which required adding additional input parameters (§2.2.1). The Kepler light curve does not have high enough signal to noise to constrain certain inputs (e.g. u_1, u_2, R_2), so we reparameterized them as a function of more accessible inputs (§2.2.2). We then used an MCMC analysis on our final set of 14 system parameters to determine the stellar and orbital properties and their posterior distributions.

2.2.1 Photometric constraints on stellar parameters

Because we do not have spectroscopic data for this system, we relied on multi-wavelength photometry and stellar evolution models for computing the stellar properties. A determination of the stellar characteristics based on multi-color photometry using the Dartmouth stellar evolution models (45) has already been carried out by the Kepler team (46, 47). However, these analyses have several drawbacks: they assumed priors on the temperature, metallicity, and mass based upon the properties of stars in the Solar neighborhood; they assumed a simplistic model for the extinction/reddening correction; and the covariances between the resulting parameters were not reported. Instead, we carried out our own fits, using a simultaneous χ^2 minimization of the Kepler photometric light curve and multi-band photometry (Figure S3) from SDSS g, r, i, z (48), 2MASS J, H, K_s (49), and WISE $W1, W2$ (50) in order to provide joint constraints on the properties of both stars and their orbital properties.

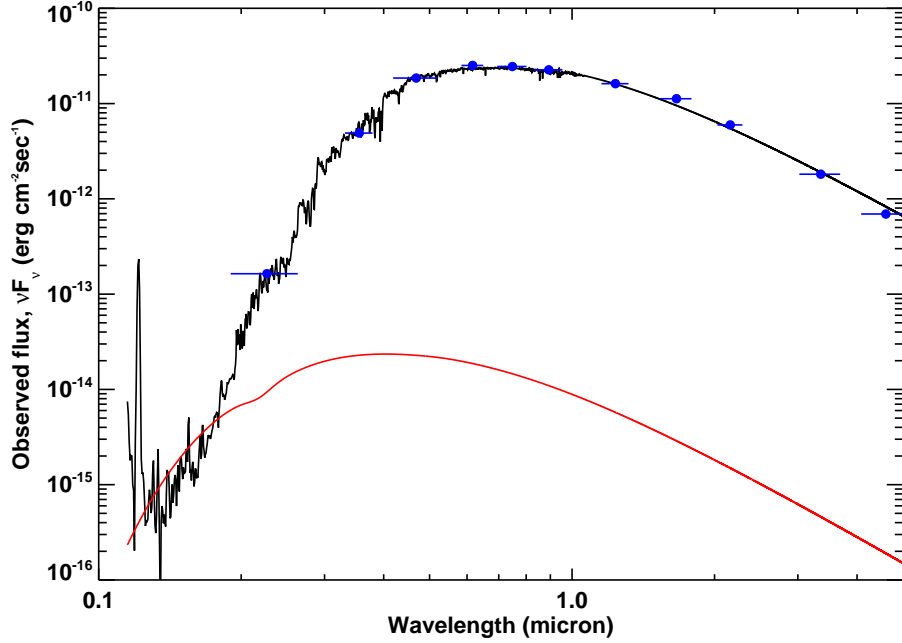


Figure S3: Spectral energy distribution of KOI-3278, computed from GALEX, SDSS, 2MASS, and WISE photometry (blue); the two shortest wavelength bands were not used in our fitting. Overplotted in black for illustration is a Pickles composite spectrum (84) for a G5V star ($T_{eff} = 5584$ K), with extinction applied, as well as a blackbody at 9950 K with the best-fit size-ratio estimated for the white dwarf (red).

This method has the advantage of self-consistently accounting for all of the stellar properties simultaneously, as well as taking into account the covariances between stellar evolution model parameters. For example, the pulse/occultation duration is a function of the density of the G dwarf and the ratio of the total binary mass to the G dwarf mass; the G dwarf density strongly correlates with the effective temperature of the star in this temperature range. Also, the height of the microlensing pulse primarily constrains the mass of the white dwarf star, given the parameters for the G dwarf and orbit (Figure S4). By fitting the multi-color photometry and light curve simultaneously we obtained a self-consistent fit to all of these constraints on the G dwarf, white dwarf, and orbital elements.

The photometric fit in multiple bands required correction for reddening. The total extinction, $A_{\lambda,max}$, we estimated from reddening maps of the galaxy (51). We assumed $E(B - V)_{max}$ has a fractional uncertainty of 3.5% based on the scatter of nearby pixel elements in the extinction map, and fixed $R_V = 3.1$. We then corrected for the finite extent of the dust layer by adding a free scale height parameter with a prior of $h_{dust} = 119 \pm 15$ pc (52). The correction for the extinction column becomes: $A_{\lambda} = A_{\lambda,max}(1 - \exp[-D \sin 10.29^\circ/h_{dust}])$, where D is the distance to the binary in parsecs – another free parameter added to the model. Finally, we added a systematic uncertainty in the absolute calibration of the photometry, σ_{sys} , which we added in quadrature to the reported photometric errors of the measured magnitudes. We let σ_{sys} vary as a free parameter, and placed a prior on its value of $\prod_i^N (\sigma_i^2 + \sigma_{sys}^2)^{-N/2}$ where $N=9$ is the

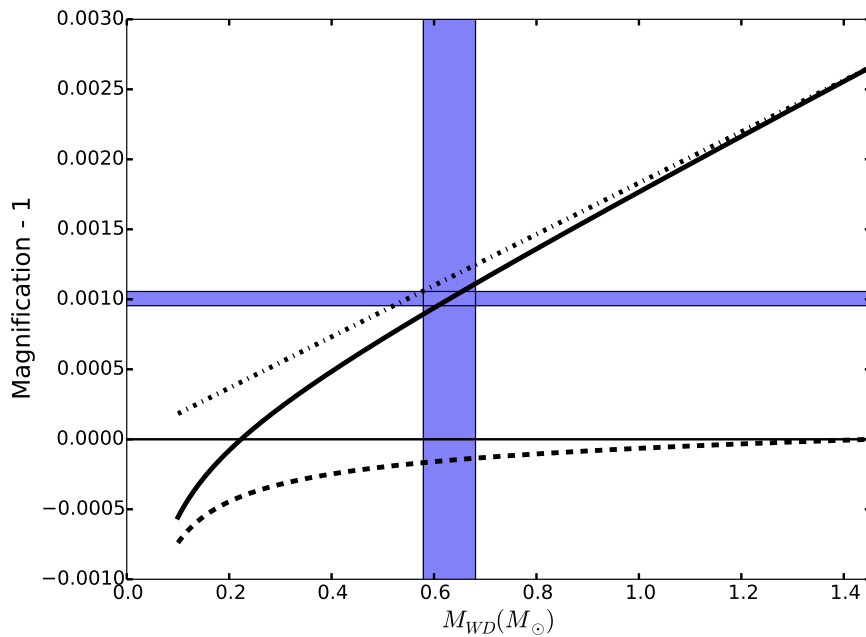


Figure S4: The “magnification” (minus one) versus mass of the white dwarf, neglecting limb-darkening of the G dwarf. The dashed-dotted curve shows the magnification versus white dwarf mass (i.e. assuming the white dwarf is transparent); the dashed curve shows the eclipse depth of the white dwarf (i.e. traditional eclipse ignoring lensing; remember more massive white dwarfs have smaller radii); and the black curve shows the predicted pulse height balancing the two effects. The blue regions show the 1σ uncertainties on the measured values.

number of photometric bands; this has the effect of giving a reduced χ^2 of order unity for the photometric fit. The median value of σ_{sys} was 2.5% in our fits.

Fitting the observed broadband magnitudes in addition to the Kepler light curve therefore required adding D , σ_{sys} , h_{dust} , and $E(B - V)_{max}$ as free parameters

For modeling the SED of the G dwarf, we used the Padova PARSEC isochrones (22), with scaled solar alpha abundances ($[\alpha/\text{Fe}] = 0$). We used this publicly available grid of stellar models computed for ages from $0.004 < t_1 < 12.59$ Gyr (spaced by 0.05 dex), metallicities from $-1.8 < [Fe/H]_1 < 0.7$ (spaced by 0.1 dex), and masses from $0.1 < M_1 < 11.75M_\odot$ (with spacings depending on age and metallicity, adaptively chosen by the isochrone model). By utilizing M_1 , $[Fe/H]_1$, t_1 to parameterize our Markov chain fits, we place a uniform prior on these parameters. We carried out linear interpolations of these parameters in the grid of stellar models to compute the radius (R_1), effective temperature, $T_{eff,1}$, $\log(g_1)$, and absolute magnitudes of the G dwarf for comparison to the multi-band photometric data, and for computation of the light curve model (the age interpolation we carried out linearly in $\log_{10}(t_1)$, although we used t_1 as the Markov chain parameter in order to avoid favoring small ages).

We checked the robustness of our results by redoing the fits with the Dartmouth isochrones (45). Unfortunately the Dartmouth isochrones have coarse sampling in metallicity below Solar metallicity (0.5 dex), so our interpolation fared poorly for sub-solar metallicity. Instead we reran our fits with only positive metallicity (using the separate fits described above), and we found that we obtained statistically identical results for both the Padova and Dartmouth isochrones with the constraint of super-solar metallicity. We conclude that our results are robust to the choice of isochrone; this is not surprising as the G dwarf star is near solar mass, where stellar evolution models are robustly constrained by comparison with our Sun. Note that the Dartmouth and Padova isochrones assume slightly different metallicities for the Sun ($Z = 0.019$ and $Z = 0.0147$, respectively), which we accounted for in our comparison.

2.2.2 Reparametrization

Some inputs to the light curve modeling are highly correlated (e.g. e , ω), while others are poorly constrained by the data due to the long Kepler cadence or low signal to noise (e.g. u_1 , u_2). We therefore reparametrized our model inputs into more insightful and independent parameters.

As discussed in §1.2, the limb darkening coefficients of the G-dwarf cannot be constrained by the data; u_1 , u_2 are thus transformed into dependent functions of the G-dwarf, which are in turn determined by the isochrones and input parameters M_1 , $[Fe/H]_1$, t_1 . The isochrones similarly determine \bar{R}_1 , and it is no longer treated as a free parameter.

We reparameterized the inclination angle in terms of the impact parameter of the white dwarf during the microlensing pulse if the orbit were circular, $b_0 \equiv (a/R_1) \cos i$.

We transformed the eccentricity and longitude of periastron to $e \sin \omega$ and $e \cos \omega$ since these are better characterized than e or ω alone; this change requires placing a prior of $1/e$ (53).

Since we could not constrain the white dwarf radius from these data, we assumed a mass-radius relation for the white dwarf given by

$$R_2(M_2) = 0.0108R_\odot \sqrt{\left(\frac{M_2}{M_{ch}}\right)^{-2/3} - \left(\frac{M_2}{M_{ch}}\right)^{2/3}}, \quad (5)$$

where $M_{ch} = 1.454M_\odot$ is the Chandrasekhar mass.

In our final fits, we constrained the age of the system to be the sum of the main-sequence lifetime of the white dwarf progenitor and white dwarf cooling time, which amounts to exchanging F_2/F_1 for the mass of the white dwarf progenitor, $M_{2,init}$ (see §3.2). Ultimately, the

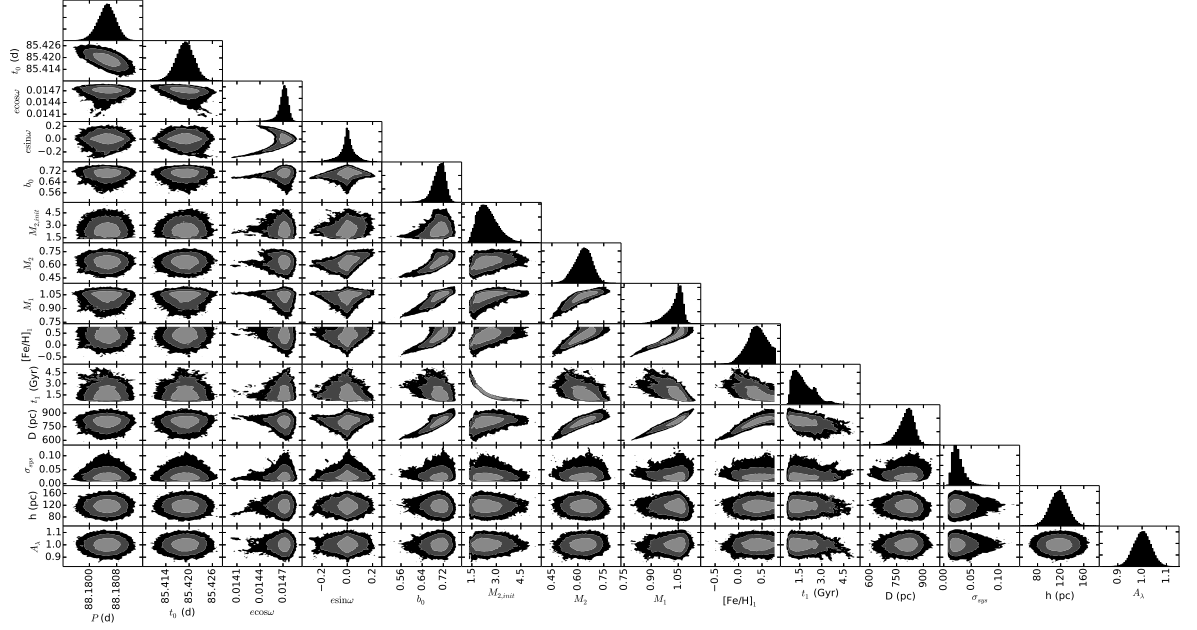


Figure S5: Contour plots showing the 1σ , 2σ , and 3σ constraints on pairs of parameters.

final set of parameters we fit for were:

$$\{P, t_0, e \sin \omega, e \cos \omega, b_0, M_2, M_{2,init}, M_1, t_1, [Fe/H]_1, \sigma_{sys}, D, h_{dust}, E(B - V)_{max}\} \quad (6)$$

for a total of fourteen free parameters.

2.3 Results

Our initial joint fits gave a reduced chi-square slightly larger than unity, so we increased the Kepler photometric error bars by a factor of 1.13 in the joint fits to produce a reduced chi-square of unity in our fit to the Kepler time-series photometry.

We ran a Markov Chain Monte Carlo simulation to constrain the fourteen model parameters using an ensemble sampler with affine-invariance (54, 55). We used a population of 50 chains and ran for a total of 100,000 generations, with maximum Gelman-Rubin statistic of 1.06.

Table 1 lists the resulting parameters derived from our simulations. Some parameters have extremely strong correlations; in particular, the measurement of the mass of the white dwarf is limited by our uncertainty in the model of the G dwarf star. Figure S5 shows the correlations between various model parameters.

3 Age Constraints

During our initial fits, we found a correlation between the age of the G dwarf and the mass of the white dwarf. This can be understood as follows: the multi-band photometry constrains the

effective temperature of the G dwarf. As stars evolve, they expand in size, but a larger radius for the G dwarf requires a larger mass of the white dwarf to reach the same microlensing pulse magnification (which scales as M_2/R_1^2). In addition, the larger radius of the G dwarf causes a longer transit duration; to fit the observed duration requires a higher impact parameter where the star is dimmer, which also works to increase the white dwarf mass needed to reach the same pulse height.

This leads to a problem with the age of the binary. To produce the observed flux ratio between the stars (derived from the occultation depth) requires a recently formed white dwarf. Yet older G dwarfs with larger radii require higher white dwarf masses to match the pulse heights; more massive white dwarfs are created by higher mass stars which have shorter main-sequence lifetimes. Hence older G dwarfs require both a short main-sequence lifetime for the white dwarf progenitor as well as a young white dwarf, producing a binary with contradictory stellar total ages.

We thus eliminated the high-mass WD and old G-dwarf solutions by requiring our binary system to be coeval. We constrained the minimum age with the spin period of the G dwarf (§3.1), and constrained the maximum age with an initial-final mass relation for the white dwarf, which determines the nuclear-burning lifetime of the white dwarf progenitor (§3.2).

3.1 Period of rotation of G dwarf and spin-down age

The light curve of KOI-3278 looks like a typical spotted star with star spots repeating every ≈ 12 days; a power spectrum peaks strongly at 12.5 days (Figure S6). Using only Q3 data, the period of rotation was measured by Reinhold et al. (56), in which they report a best-fit period of 12.36 ± 0.05 days, consistent with our results from all 17 quarters.

The rotation period can be used to estimate the age of the G dwarf. We estimated the age of the star based on the observed spin-down of stars as they age; so-called “gyrochronology.” We used the calibrations of this relation by (57) to estimate the age of this star, which we found to be $t_{spin,1} = 0.89 \pm 0.15$ Gyr. We used this constraint only as the minimum age of the system, however, to allow for the possibility that the G-dwarf was spun up via mass transfer during the white dwarf’s formation.

3.2 Breaking the M_2 , Age Degeneracy

To eliminate the models with contradictory ages, we placed a constraint on the age of the G dwarf by adding together the cooling age of the white dwarf and the nuclear-burning lifetime of its progenitor. However, the progenitor mass has some uncertainty due to uncertainties in the initial-final mass relation of white dwarfs, which is compounded by the fact that the common-envelope evolution of this system would have modified the core mass of the white dwarf progenitor. After surveying the literature on the initial-final mass relation of white dwarfs (58–62), and running a suite of binary stellar evolution models (described below), we found that most data and models lay within 10% of the final mass given by the initial-final mass relation found by Kalirai (59). Consequently, we allowed both the initial mass of the white dwarf, $M_{2,init}$, and the final mass, M_2 , to vary, and placed a Gaussian prior on M_2 to lie within 10% of the Kalirai relation, which amounts to adding to the χ^2 : $(M_2 - 0.109M_{2,init} - 0.394)^2 / (0.1M_2)^2$.

We computed the nuclear-burning lifetime of the white dwarf progenitor, t_2 , from the Padova models, and then set the cooling time of the white dwarf equal to $t_{cool} = t_1 - t_2$. The cooling time and mass of the white dwarf was then used to compute its Kepler magnitude (as described below), which was then used to fit the depth of the occultation. This procedure has the effect of

requiring both stars to have the same age, but allowing for some uncertainty in the initial mass of the white dwarf progenitor. In doing so, we exchanged F_2/F_1 for $M_{2,init}$ as a free parameter in the model. This procedure eliminated the unphysical cases of large white dwarf masses in old systems.

3.2.1 WD Cooling

We can derive the absolute magnitude of the white dwarf star in the Kepler band from the flux lost as the white dwarf completely disappears behind the G-dwarf during occultation; we can then use this to constrain the age and luminosity of the white dwarf based on white dwarf cooling models. We use the cooling models computed by Bergeron and collaborators (23, 63–65), made available on their web site¹. We performed a linear interpolation in the mass and log cooling age of the white dwarf to obtain the absolute magnitudes, luminosity, and effective temperature of the white dwarf. The absolute magnitude of the white dwarf in the Kepler band was computed by transforming the absolute magnitudes in the SDSS g , r and i bands: $K_p = 0.25g + 0.75r$ for $(g - r) \leq 0.3$ and $K_p = 0.3g + 0.7i$ for $(g - r) > 0.3$ (66).

We found a white dwarf age of $t_{cool} = 663 \pm 60$ Myr; equivalent ages were found for both Helium and Hydrogen atmosphere models. The effective temperature of the white dwarf is $T_{eff,2} = 9960 \pm 730$ K and its luminosity is $L_{WD} = (1.2 \pm 0.23) \times 10^{-3} L_{\odot}$; hence the small depth of the occultation in the Kepler band.

4 Blends

It is possible that the flux from another star (or stars) can be blended with the flux of the binary star, thus affecting our fit to the photometry and light curve. To test this, we added to our separate-fit model two components: 1) a bound blend star with the same metallicity and age as the G dwarf; 2) a blend star along the line of sight to the binary, contained within the Kepler photometry aperture.

For the first component, we added the flux of a second star to the multi-color photometry, drawing from the Padova isochrones as for the G dwarf, and we also included its effect on the pulse height and occultation depth.

For the second component, the contamination within the Kepler aperture can be estimated by combining the location of other stars in other photometric surveys with the Kepler point spread function to compute the flux contamination with the target aperture. The Kepler pipeline carries out this analysis, and finds that the contamination is between 4-8%, depending on the quarter of data that is used. We added the contamination flux to both our models to account for the slight reduction in the pulse height/occultation depth due to contamination that varies with quarter.

We re-ran the Markov chain fit including the mass of the third bound star, M_3 , as an additional free parameter. We found that a bound star must be an M dwarf, $M_3 = 0.4 \pm 0.2 M_{\odot}$, to be consistent with the data, and would contribute only $1.4^{+3.7}_{-1.0}\%$ to the Kepler band flux. However, the M dwarf would contribute more significantly to the 2MASS/WISE bands and thus skew the effective temperature of the G dwarf to be somewhat hotter, and thus somewhat more massive, $M_1 = 1.07^{+0.04}_{-0.05} M_{\odot}$. This would imply a slightly higher white dwarf mass, $M_2 = 0.68^{+0.05}_{-0.06} M_{\odot}$, about 1σ different from the fit without a third star. The slightly higher mass for the white dwarf

¹<http://www.astro.umontreal.ca/~bergeron/CoolingModels/>

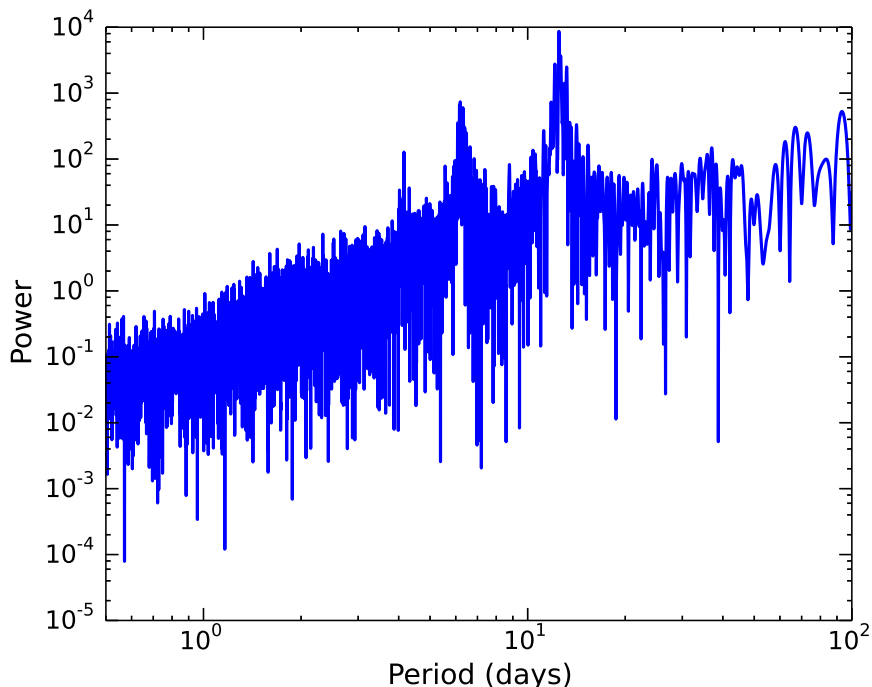


Figure S6: Frequency-power spectrum of KOI-3278, showing a strong peak at 12.5 days which we infer to be the rotational period of the G dwarf.

would produce a slightly higher mass for its progenitor, as well as a slightly smaller cooling age, and thus a slightly smaller overall age for the system. Higher contrast imaging and/or high resolution spectroscopy may be able to place stronger constraints on the presence of a third bound star in the system; however, the current constraints are strong enough that the mass derived for the white dwarf is not strongly affected by the third star.

5 Binary stellar evolution models and dynamical constraints on the presence a bound third star

We carried out an initial exploration of the possible origin of this system using the BSE code (67–69) to model the evolution of this system as a function of time. At the current orbital period, the G dwarf should have orbited within the surface of the red giant progenitor of the white dwarf, ejecting the outer envelope of the star; this is referred to as the “common envelope phase” (70, 71). We used the calibration of the common-envelope evolution parameters derived empirically (60), and carried out simulations with a range of initial masses and separations. As an example of these simulations, we found that the final conditions of this system could be achieved if the initial masses were $M_{2,init} \approx 2.5M_{\odot}$, $M_1 \approx 1M_{\odot}$ and the initial period was $P_0 \approx 1295$ days, corresponding to an initial semi-major axis of $a_0 \approx 3.5$ AU (we used $\alpha_{CE} = 0.3$ and $\lambda = 0.2$ in this simulation). The mass transferred during the Roche-lobe

overflow and common envelope phase would be $\Delta M_1 = 0.008 M_\odot$, sufficient to spin up the G dwarf. The common envelope phase would start on the second asymptotic giant branch of the white dwarf progenitor, at an age of ≈ 0.8 Gyr, and result in a final mass of the white dwarf of $M_2 \approx 0.65 M_\odot$, consistent with the model constraints, and slightly less massive than the final mass of $0.69 M_\odot$ had the star evolved as a single star. As the common envelope phase causes rapid merging of the two stars before ejection of the evolved star’s envelope, the final period is very sensitive to the initial period; the outer period thus has to be fine-tuned, and hence this sort of binary is expected to be rare (72–79).

The possibility of a third body in the system is potentially constrained by the dynamical interactions of the 3 bodies due to the eccentric-Kozai mechanism (80–82). The observed eccentricity of the binary is small, $e_1 \approx 0.032$, which indicates that it was probably circularized during the common-envelope phase, and avoided dynamical growth of its eccentricity with a third body, post-circularization. Since the timescale for growth of the eccentricity depends upon the quadrupole timescale, we estimate that the third body should satisfy $(a_2/AU)^3/(M_3/M_\odot) > 1.7 \times 10^8$ so that the Newtonian quadrupole timescale is less than the white dwarf cooling timescale. Thus, if the third body has a mass of $M_3 \approx 0.4 M_\odot$, the semi-major axis should be larger than $a_2 > 748$ AU, with an orbital period longer than 14,000 yr. This is at about a separation of $1''$ (at quadrature), and thus the presence of a third body could be constrained with future high-contrast imaging and dynamical simulations.

The value of this system can be seen when comparing with the other white dwarf-main sequence eclipsing binaries found to date (Figure S7). KOI-3278 has the most massive companion star, as well as the longest period of all such systems. The longer period binaries are more difficult to find with ground-based surveys, and also have a lower probability of eclipse/occultation/microlensing. The cooler companion stars are easier to find due to their larger color difference to their companion white dwarf stars. KOI-3278 could only be found with continuous coverage and with high photometric sensitivity.

6 Predictions for future observations

Based on our Markov chain analysis, we found that the velocity semi-amplitude of the G dwarf should be $K_1 = 21.5 \pm 1$ km/s. The parallax of the system should be $\pi = 1.24_{-0.05}^{+0.08}$ milliarcseconds (mas) with a reflex motion of $\alpha = 0.22 \pm 0.08$ mas. The expected parallax measurement uncertainty for a $G = 15$ (Gaia magnitude) star is 0.02-0.03 mas (83), so the parallax precision from Gaia should improve upon our analysis significantly, and enable another constraint on the mass of the white dwarf star.

We simulated the flux ratio of the white dwarf to the G dwarf as a function of wavelength, which we find reaches $\approx 5\%$ at 0.25 micron, increasing to 60% at 0.15 micron (although the absolute flux drops significantly towards shorter wavelength). We found that single occultation measurements in the ultraviolet could have similar signal-to-noise as the combined Kepler occultations, and allow a measurement of the temperature of the white dwarf, breaking the size-temperature degeneracy that required us to use a mass-radius relation for the white dwarf. For instance, we found that observations using the Hubble Space Telescope at 0.2-0.4 micron (with the G280 grating on the Wide Field Camera III) could achieve a S/N of ≈ 25 with observation of a single occultation (if it were photon-noise limited).

Acknowledgments: We acknowledge the dedication and hard work of the Kepler team in obtaining and analyzing the data used in our analysis. This research has made use of the VizieR catalogue access tool, CDS, Strasbourg, France. This research has made use of NASA’s Astrophysics Data System.

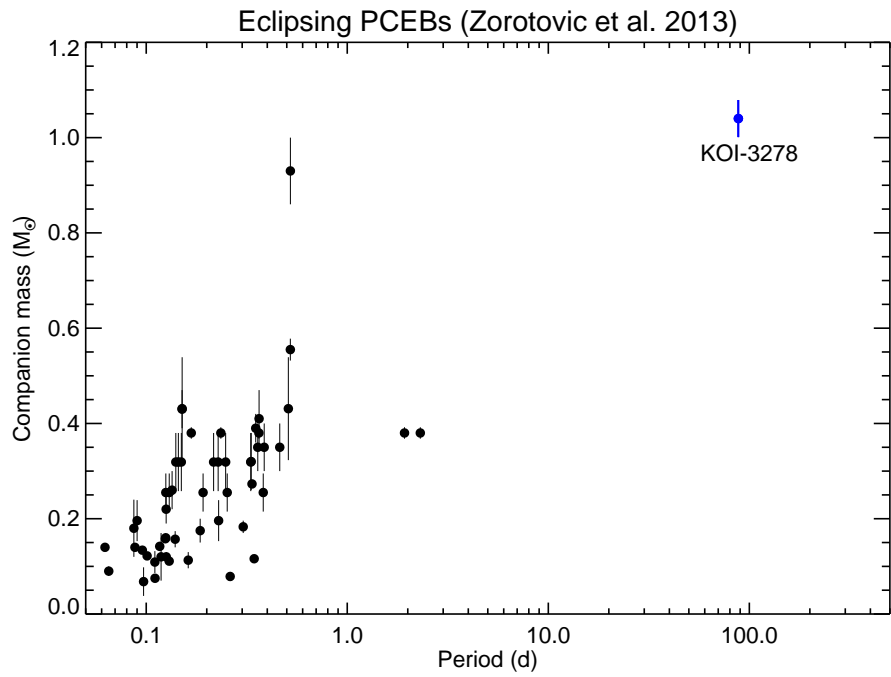


Figure S7: Mass-period distribution of known white dwarf-main sequence post common envelope eclipsing binaries.